DOI: 10.13009/EUCASS2023-321
Aerospace Europe Conference 2023 – 10TH EUCASS – 9TH CEAS

Pressure Model of Buzz Oscillation in a Ramjet Intake

*Manami FUJII *†, Tetsuya SATO *, Atsushi HASHIMOTO ‡, and Hideyuki TAGUCHI ‡*
** Waseda University*
3-4-1 Okubo, Shinjuku-ku, Tokyo 169-8555, Japan
m-fujii@moegi.waseda.jp – sato.tetsuya@waseda.jp
‡ Japan Aerospace Exploration Agency
7-44-1 Jindaiji-Higashimachi, Chofu-shi, Tokyo 182-8522, Japan
hashimoto.atsushi@jaxa.jp - taguchi.hideyuki@jaxa.jp
† Corresponding Author

Abstract
The buzz characteristics occurring in ramjet intakes vary significantly depending on the freestream Mach number. In the case of a high freestream Mach number, the flow inside the intake becomes supersonic during the buzz, so the well-known acoustic resonance model is not applicable. In this research, a new buzz model was constructed to apply to this type of the buzz by combining the mass conservation law and the governing equations of the moving shock wave. As a result of applying this model to the pressure increasing period of the buzz, the model output agreed with the CFD result, quantitively.

Nomenclature

a	: Speed of the sound	R	: Gas constant
A	: Cross sectional area	T	: Static temperature
f	: Buzz frequency	u	: Flow velocity (x-axis direction)
IOR	: Intake opening ratio	U_s	: Moving speed of the shock wave
L	: Length of the intake	V	: Volume of the intake flow path (From the cowl tip to the nozzle entrance) ($= 3.03 \times 10^{-4}\ m^3$)
M	: Mach number		
$\dot{m}$	: Mass flow rate		
M_s	: Shock Mach number	Δt_{model}	: Time-step of model calculation
NOR	: Nozzle opening ratio	κ	: Specific heat ratio
p	: Static pressure	ρ	: Density

Subscripts

0	: Stagnation value	*back*	: In front of the nozzle (P2 shown in Fig. 1)
1	: Upstream of the terminal shock wave		
2	: Downstream of the terminal shock wave	*bleed*	: Bleeding from the two bleeding holes
ave	: Average value inside the intake (dividing the result of volume integral by the volume)	*in*	: Inflow
		n	: Running index in the time direction
		out	: Outflow
		throat	: Nozzle throat

DOI: 10.13009/EUCASS2023-321

1. Introduction

Developments of hypersonic passenger airplanes are being accelerated in recent years [1][2] in order to deal with the acceleration of the global business development. In Japan, Japan Aerospace Exploration Agency, JAXA, and universities are conducting research to develop the hypersonic passenger airplane using the pre-cooled turbojet engine [3] and most of the elemental technologies have been acquired. However, the integrated control technologies of the airframe and the engine have not been established yet. Therefore, High Mach Integrated Control Experiment, HIMICO, has been planned to demonstrate these technologies. This is the hypersonic flight experiment using the S-520 sounding rocket. In this experiment, one ramjet engine will be used.
The performance of the ramjet intake is known to be enhanced by increasing the intake back pressure. However, the excessively high intake back pressure is known to induce a buzz, which is the self-excited oscillation of the shock wave. This phenomenon causes the severe pressure oscillation inside the engine and can result in the structural damage to the engine and the aircraft. Therefore, in order to avoid the buzz itself and to prevent the resonance with the engine or the airframe when the buzz occurs, it is necessary to clarify the buzz mechanism and to construct buzz models.
The investigations of the buzz have been widely conducted by many researchers. In 1984, Newsome [4] considered the buzz mechanism to be attributed to the reflection of a compression wave and an expansion wave and proposed,

$$f_N = \frac{a}{4L}\left(1 - {M_{ave}}^2\right)(2N-1), \quad N = 1,2,3,\cdots \tag{1}$$

where a is the speed of the sound, L is the length of the intake and M_{ave} is the average Mach number. This equation represents the acoustic resonance in the intake duct. This kind of acoustic resonance models were verified by many researchers and reported the agreement with the experimental or the numerical results [4]-[9]. However, Tan et al. [10] indicated that the acoustic resonance model cannot be applied to the buzz occurring in the hypersonic intake because the supersonic region temporarily exists and prevents the propagations of the acoustic waves. The disagreement of the hypersonic intake buzz frequency with that obtained by the acoustic resonance model is also reported by Zhang et al. [11]. Under these circumstances, the construction of new buzz models which can be applied to the buzz whose flow becomes supersonic is required. In 2021, Devaraj et al. [12] newly defined the length scale of the acoustic resonance model based on the type of the buzz to enable the adaptation of the acoustic resonance model for the buzz whose flow becomes supersonic. This newly defined acoustic resonance model can estimate the buzz frequency over a wide range of freestream Mach number within an error of 20 %, but the physical validity has not been sufficiently taken into account. In 2020, Sekar et al. [13] constructed the equation which can estimate the buzz frequency from the isolator inlet Mach number, the freestream Mach number, the throttling ratio, the isolator length, and the stagnation acoustic speed. However, this is a semi-empirical formula, and the discussion regarding the physical laws has not been adequately addressed. In 2009, Tan et al. [10] focused on the phenomenon that the mass of the air stored inside the intake increases because of the difference between the inflow rate and the outflow rate during the pressure increasing period of the buzz, and calculated the length of the pressure increasing period by adapting the mass conservation law to the intake. This model is physically coherent, but most of the variables in this model need to be estimated by CFD or experiments. This is because the mechanism of the buzz has not been revealed yet. In summary, some of the attempts have been made to construct the new buzz frequency models, but a model which is physically validated and also does not require the CFD or the experimental data has not been constructed yet.
Therefore, the investigation of the buzz mechanism and the construction of a more practical and more physically based model have been conducted in our research group. In the previous research [14], the effects of the outflow rate (exit nozzle throat height) on the buzz characteristics were investigated, numerically. As a result, the dependence of the moving speed of the shock wave on the outflow rate was observed during the second half of the pressure increasing period, but not observed in the first half of the period. Therefore, the mechanism of the shock wave movement was suggested to be different between the first half and the second half of the pressure increasing period. Based on this finding, the present study constructs a new buzz model which considers the movement of the shock wave and divides the pressure increasing period into the two periods.

2. Methods

2.1 Model

The ramjet intake for HIMICO is investigated in this paper. As shown in Fig. 1, it is the rectangular mixed-compression intake consisting of the ramp section, the diffuser, the duct, and the variable geometry nozzle and the design Mach

DOI: 10.13009/EUCASS2023-321

number is 5. The pitot tube and the injector exist in the diffuser and the duct. Figure 2 is the enlarged figure of the ramp section. As shown in this figure, the ramp section consists of the 1st ramp, the 2nd ramp, the 3rd ramp, the cowl, and the side walls. The area over the 2nd ramp and the 3rd ramp is the plenum chamber. The boundary layer is extracted from the slit between the 2nd ramp and the 3rd ramp and is exhausted from the bleed holes. In this intake, the 2nd ramp, the 3rd ramp, and the exit nozzle are movable. The intake opening ratio (*IOR*) and the nozzle opening ratio (*NOR*) are defined by:

$$IOR = \frac{H2}{H1}, \tag{2}$$

$$NOR = \frac{H5}{H1}. \tag{3}$$

In this paper, *IOR* and *NOR* are fixed at 0.43 and 0.34, respectively. The dimensions and the angles of the intake are listed in Table 1 and Table 2.

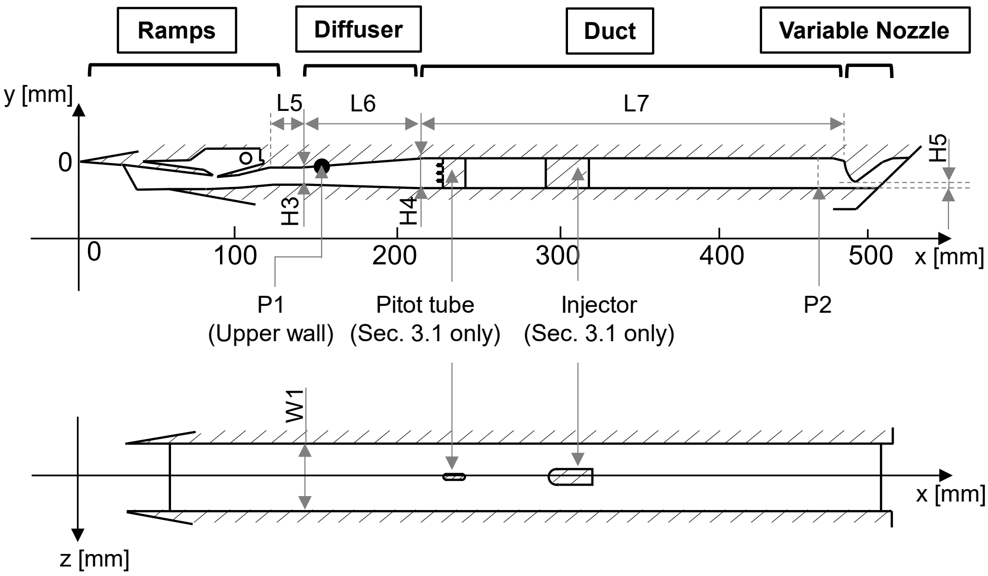

Figure 1: Schematic of the ramjet intake for HIMICO

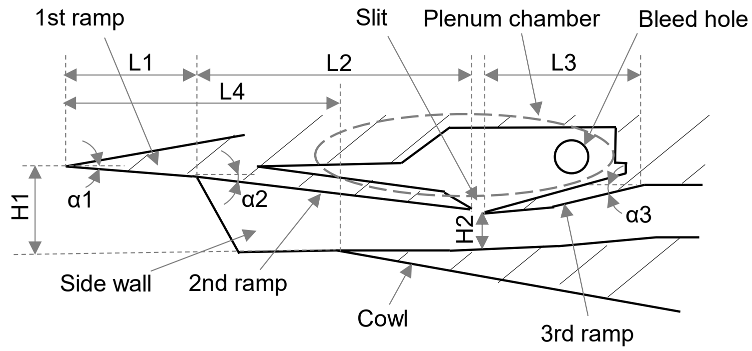

Figure 2: Enlarged figure of the ramp section

DOI: 10.13009/EUCASS2023-321

Table 1: Dimensions of the ramjet intake

	L1	L2	L3	L4	L5	L6	L7	H1	H2	H3	H4	H5	W1
Dimension	26.9	57.9	32.7	56.8	21.3	80.0	258.9	17.8	7.6	10.5	19.5	6.0	43.0

Units are [mm]

Table 2: Angles of the intake ramps from the x-axis

	α1	α2	α3
Dimension	5.0	6.7	14.3

Units are [deg]

2.2 Numerical method and conditions

The numerical simulations were conducted using JAXA Supercomputer System Generation 3 (JSS3). The calculation solver was Fast Aerodynamic Routines, FaSTAR[15], developed by JAXA. The numerical methods employed in this paper are listed in Table 3. The overview of the calculation grids and the information of the boundary conditions are shown in Fig. 3. As shown in this figure, the flow around the intake entrance and inside the intake was calculated. The freestream conditions are shown in Table 4. The Reynolds number was calculated using the intake entrance height, H1, as the characteristic length.

Table 3: Numerical methods

Dimension	3D
Turbulence Model	DDES (SST-2003sust [16])
Inviscid Flux Calculation	SLAU [17]
Accuracy	2nd Order (MUSCL Scheme)
Time Integration	LU – SGS Model
Limiter	Hishida (van Leer) [18]

Table 4: Freestream conditions

Mach number	3.4
Total temperature	300 K
Total pressure	374 kPa
Reynolds number	4.02×10^5

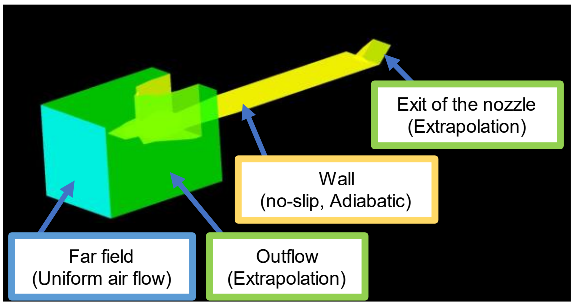

Figure 3: Boundary conditions

DOI: 10.13009/EUCASS2023-321

2.3 Experimental setup

The experiment was conducted using the supersonic wind tunnel at JAXA Sagamihara Campus. The freestream conditions were the same with CFD. The unsteady static pressure was measured using the unsteady pressure sensor, XCS-190 (Kulite), and the data logger, NR-HA08 (Keyence). The pressure measurement point, P1, is shown in Fig. 1. During the test, *IOR* was fixed at 0.43 and *NOR* was decreased from 0.50 to 0.17 stepwise. In this paper, the data with *NOR* = 0.29 is used.

3. Numerical results

3.1 Verification and the validation of the numerical results

In this section, the verification and the validation of the numerical simulation are performed. The value of *NOR* was set at 0.31 in CFD. First, the grid refinement test was conducted by preparing the medium grid and the fine grid. The unstructured grids were used in this calculation and the information of the grids is shown in Table 5. The y+ was set at around 1.7 in both grids. The two simulations were conducted with $\Delta t = 2.6 \times 10^{-7}$ s. The static pressure waveforms at P1 obtained by CFD are shown in Fig. 4. As shown in this figure, the static pressure waveforms obtained by these two grids agreed well with each other. Therefore, the medium grid is sufficient in this simulation and is chosen in this paper.
Next, the time-step sensitivity test was conducted using the medium grid. The value of the time-step is listed in Table 6 and the static pressure waveforms at P1 obtained by these three simulations are shown in Fig. 5. Clearly, the waveform of the static pressure is not significantly affected by the time-step value. Therefore, $\Delta t = 2.6 \times 10^{-7}$ s is sufficient in this simulation, and this value is determined to be used in this paper.
Finally, the result of the numerical simulation is compared with that of the experiment (EFD) as shown in Fig. 6. This figure indicates that the static pressure waveform obtained by CFD and the experiment agreed well with each other. Therefore, the buzz is accurately simulated by CFD. Hereinafter, the medium grids and $\Delta t = 2.6 \times 10^{-7}$ s are employed in CFD.

Table 5: Grids information

	Cell number	**Point number**
Medium	77 million	23 million
Fine	173 million	56 million

Table 6: Time-step information

	Time-step [s]
T1	5.2×10^{-7}
T2	2.6×10^{-7}
T3	1.3×10^{-7}

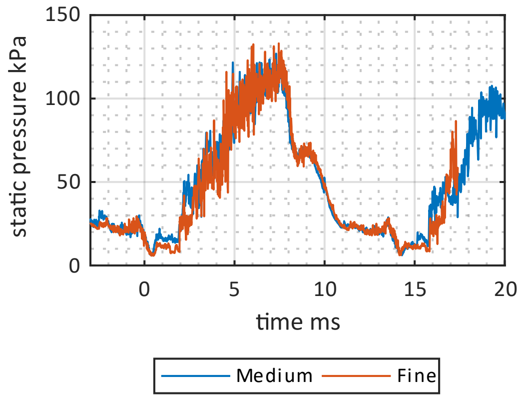

Figure 4: Static pressure waveform (Grid refinement test, P1)

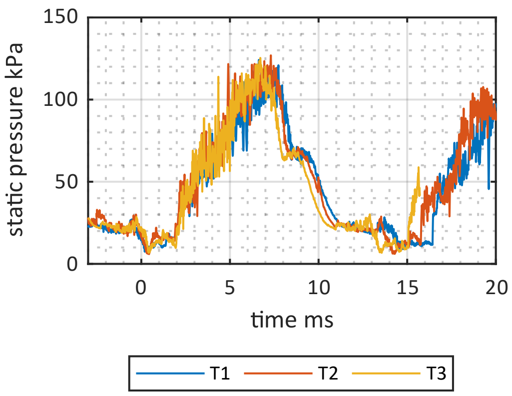

Figure 5: Static pressure waveform (Time-step sensitivity test, P1)

DOI: 10.13009/EUCASS2023-321

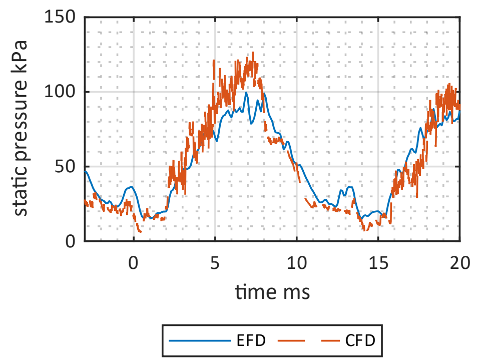

Figure 6: Static pressure waveform (Comparison between EFD and CFD, P1)

3.2 Overview of the buzz phenomenon

From this section, the pitot tube and the injector were removed from the calculation grids to make the phenomenon simple. The results of CFD (the intake back pressure (p_{back}), the average static pressure inside the intake (p_{ave}), the inflow rate, the outflow rate, the bleeding airflow rate, and the position of the head of the terminal shock wave) are shown in Fig. 7 to Fig. 9. In this paper, the value indicated with the subscript, *back*, is obtained as the cross-sectional averaged value at P2 shown in Fig. 1. The value indicated with the subscript, *ave*, is calculated by dividing the result of the volume integral between the cowl tip and the nozzle entrance by the volume of the intake flow path between the cowl tip and the nozzle entrance. The position of the head of the terminal shock wave was judged by both the distribution of the static pressure at 1 mm away from the sidewall surface and the Schlieren images.
As indicated in Fig. 7, a cycle of the buzz is divided into the pressure increasing period and the pressure decreasing period in this paper. In the pressure increasing period, the inflow rate exceeds the outflow rate (Fig. 8), so p_{ave} increases as shown in Fig. 7. In this paper, the pressure increasing period is further divided into the 4 periods based on the waveform of p_{back} and the position of the terminal shock wave. At the beginning of the pressure increasing period, the time lag exists from the inflow rate becomes positive (-0.9 ms) till p_{back} starts to increase (0.4 ms) as shown in Fig. 7 and Fig. 8. This time lag is named to be I1. Then, p_{back} starts to increase sharply as shown in Fig. 7 and this is the beginning of I2. During most part of I2, p_{back} is kept almost constant at the medium value, but the terminal shock wave moves upstream as shown in Fig. 9. At 2.5 ms, p_{back} restarts to increase as shown in Fig. 7. This is the start of I3. At this moment, the head of the terminal shock wave precisely reaches the root of the 3rd ramp (x = 120.0 mm) as shown in Fig. 9. During I3, the head of the terminal shock wave moves upstream under the 3rd ramp, but the moving speed of the terminal shock wave is smaller than that of I2 as shown in Fig. 9. During I4, the head of the terminal shock wave moves upstream under the 2nd ramp, and finally, the terminal shock wave is expelled from the intake and the inflow rate decreases drastically as shown in Fig. 8. This is the pressure decreasing period. In the pressure decreasing period, the reverse flow occurs from the intake entrance as depicted by Fig. 8 and as a result, the static pressure inside the intake decreases as shown in Fig. 7. When the static pressure inside the intake becomes sufficiently low, the shock wave retreats into the intake and the buzz phase changes into the pressure increasing period again.

DOI: 10.13009/EUCASS2023-321

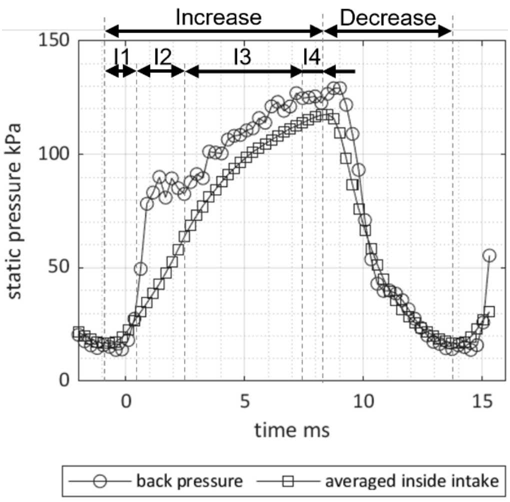

Figure 7: Time variation of the surface averaged static pressure

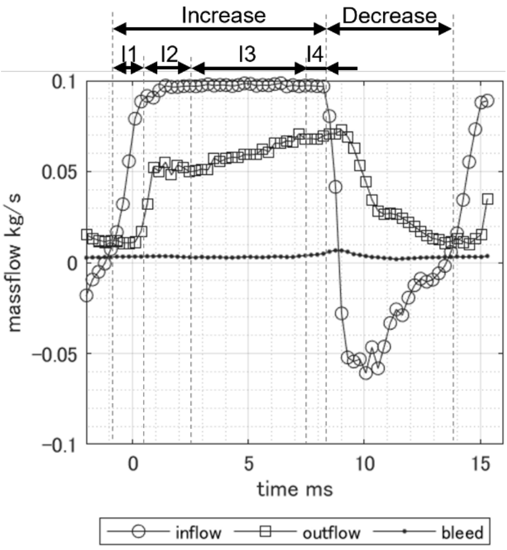

Figure 8: Time variation of the mass flow rate

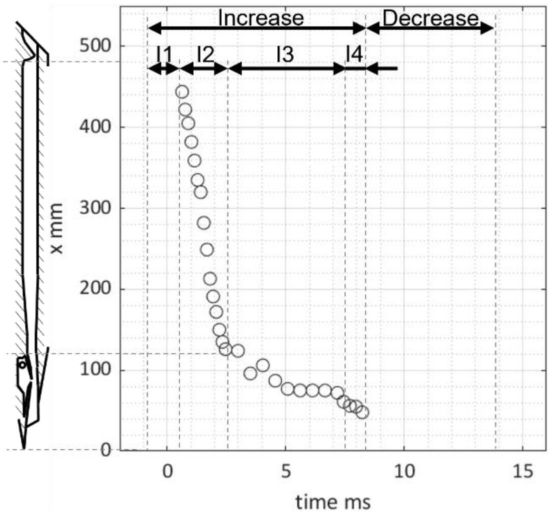

Figure 9: Time variation of the shock head position

Next, the buzz characteristics are discussed from the viewpoint of the pressure distribution and the shock wave structure. The contour view of the static pressure and the Schlieren images are shown in Fig. 10 and Fig. 11. In the Schlieren images, the black region indicates the areas where the slope of density in the x-direction is positive, while the white region indicates the areas where the slope is negative. The distribution of the surface averaged static pressure during I2 and I3 are shown in Fig. 12 and Fig. 13. In this paper, the surface averaged values were calculated by dividing the result of surface integral by the cross-sectional area.

During I2, the high-pressure region expands from the rear part of the intake towards the upstream direction because the inflow rate exceeds the outflow rate as shown in Fig. 10(a) and (b). However, the static pressure of the high-pressure region does not increase very much as depicted by these two figures. In this period, the terminal shock wave moves upstream accompanied with the expansion of the high-pressure region as shown in Fig. 11(a) and (b). The terminal shock wave is the normal shock wave at first, but it changes into the shock train as shown in these two figures. The movement of the terminal shock wave can be also observed in Fig. 12 because the surface averaged static pressure rises at the position of the head of the terminal shock wave. Also, the change of the terminal shock wave from the normal shock wave to the shock train appears as the bluntness of the pressure rise after 1.4 ms in Fig. 12. During I3, the high-pressure region further expands and the terminal shock wave further moves upstream. In this period, the movement of the terminal shock wave is slower than I2 as indicated in Fig. 13, but the static pressure of the high-pressure region increases (Fig. 10(b) and (c)).

DOI: 10.13009/EUCASS2023-321

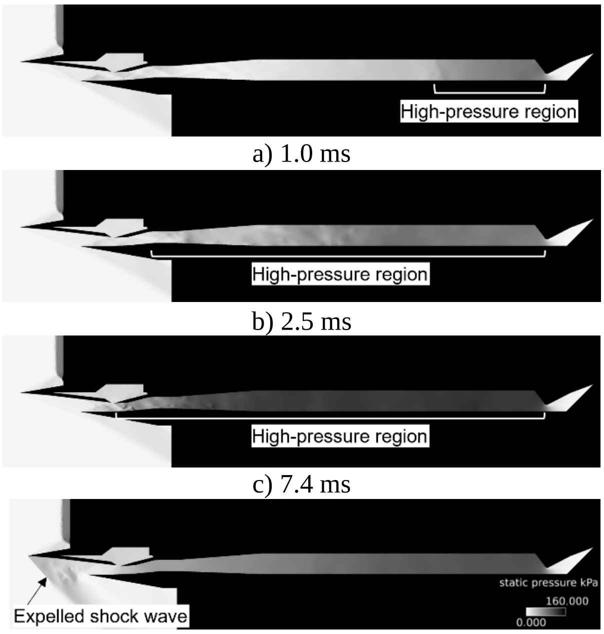

a) 1.0 ms

b) 2.5 ms

c) 7.4 ms

d) 9.5 ms

Figure 10: Static Pressure distribution (Symmetric surface)

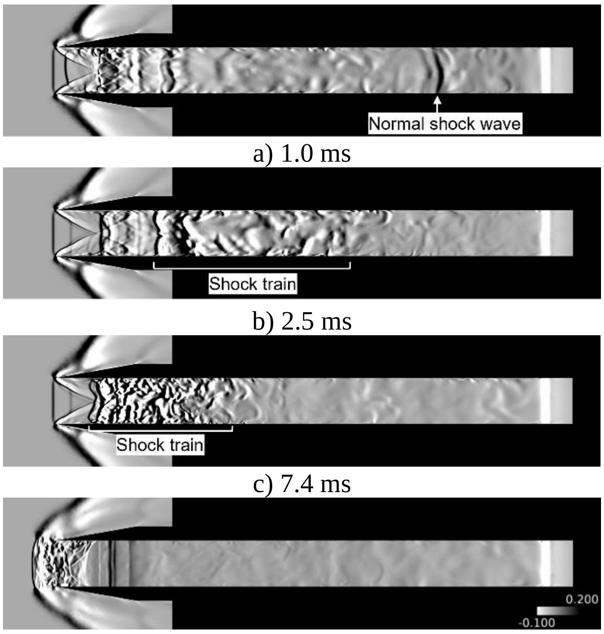

a) 1.0 ms

b) 2.5 ms

c) 7.4 ms

d) 9.5 ms

Figure 11: Schlieren images (Density gradient of CFD result, y = -11.7)

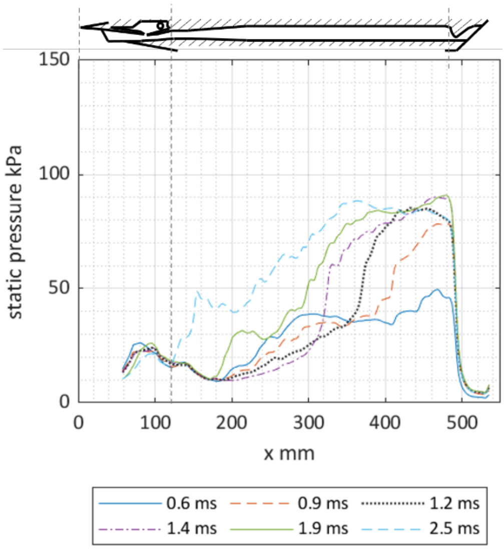

Figure 12: Distribution of the surface averaged static pressure (I2)

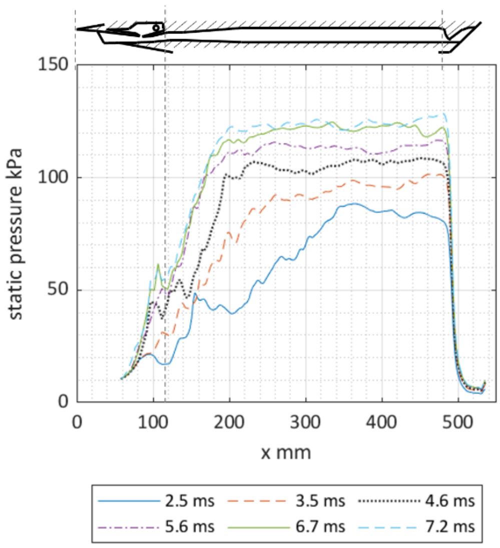

Figure 13: Distribution of the surface averaged static pressure (I3)

4. Modelling of pressure increasing period

In the previous research, the effects of *NOR* on the buzz characteristics were investigated numerically [14]. The change of *NOR* is the synonym to the change of the outflow rate. In the research, the moving speed of the terminal shock wave and the increasing speed of p_{back} were found to be unaffected by the outflow rate during I2. On the other hand, both the speed of the terminal shock wave movement and the increasing speed of p_{back} became larger with the smaller outflow rate during I3. Therefore, the mechanisms of the movement of the terminal shock wave and the rise of p_{back} were suggested to be different between I2 and I3. Taking the characteristics of I2 and I3 into consideration, they seem to be the governing equations of the moving normal shock wave and the mass conservation law, respectively. In this section, the time variations of the shock wave position and the static pressure are modelled by these two theories and these hypotheses are verified.

DOI: 10.13009/EUCASS2023-321

4.1 Modelling the average static pressure inside the intake

In this section, p_{ave} and ρ_{ave} are modelled by applying the mass conservation law and the equation of state to the intake. The equation of the mass conservation law used to calculate ρ_{ave} is represented as follows:

$$\rho_{ave}{}^{n+1}V = (\dot{m}_{in}{}^{n} - \dot{m}_{out}{}^{n} - \dot{m}_{bleed}{}^{n})\Delta t_{model} + \rho_{ave}{}^{n}V, \tag{4}$$

where n is the running index in the time direction. In this calculation, $\dot{m}_{in}$ and $\dot{m}_{bleed}$ are acquired by CFD and $\dot{m}_{out}$ is calculated by the following equation considering that the nozzle throat is choking:

$$\dot{m}_{out} = \frac{p_{back}A_{throat}}{\sqrt{RT_{0\,back}}}\sqrt{\kappa}\sigma^*, \tag{5}$$

where σ^* is defined by:

$$\sigma^* = \left(\frac{2}{\kappa+1}\right)^{\frac{\kappa+1}{2(\kappa-1)}} = 0.579. \tag{6}$$

In Eq. (5), $T_{0\,back}$ is obtained by CFD and p_{back} is calculated by the methods explained in Sec. 4.2. p_{ave} is calculated using the equation of state from ρ_{ave} obtained by Eq. (4) and T_{ave} obtained by CFD. p_{ave} at the beginning of I1 obtained by CFD is set as the initial condition in this calculation. The pressure increasing period is considered to be end and the calculation is stopped when p_{ave} calculated by the model reaches around the maximum value of p_{ave} obtained by CFD.

4.2 Modelling the intake back pressure and the shock wave position

In this section, p_{back} and the shock wave position during the pressure increasing period are modelled. During I1, p_{back} is kept almost constant as shown in Fig. 7. Therefore, p_{back} during I1 is fixed in this model and p_{ave} at the beginning of I1 obtained by CFD is substituted. The time that the buzz phase changes into I2 is also obtained by CFD and is 0.629 ms.

During I2, the governing equations of the normal shock wave moving at velocity, Us, is considered. These equations are established by considering the control volume moving with the normal shock wave as shown in Fig. 14. By assigning the subscripts 1 and 2 to the physical properties upstream and downstream of the normal shock wave, respectively, the governing equations are established as follows:

$$\rho_1(U_s + u_1) = \rho_2(U_s + u_2), \tag{7}$$

$$p_1 + \rho_1(U_s + u_1)^2 = p_2 + \rho_2(U_s + u_2)^2\,, \tag{8}$$

$$\frac{\kappa}{\kappa-1}\frac{p_1}{\rho_1} + \frac{1}{2}(U_s + u_1)^2 = \frac{\kappa}{\kappa-1}\frac{p_2}{\rho_2} + \frac{1}{2}(U_s + u_2)^2. \tag{9}$$

By introducing the shock Mach number,

$$M_s = \frac{U_s + u_1}{a_1}, \tag{10}$$

the following equations can be obtained by Eq. (7) to Eq. (9).

$$\frac{u_1 - u_2}{a_1} = \frac{2}{\kappa+1}\left(M_s - \frac{1}{M_s}\right) \tag{11}$$

DOI: 10.13009/EUCASS2023-321

$$\frac{p_2}{p_1} = \frac{2\kappa {M_s}^2 - (\kappa - 1)}{\kappa + 1} \tag{12}$$

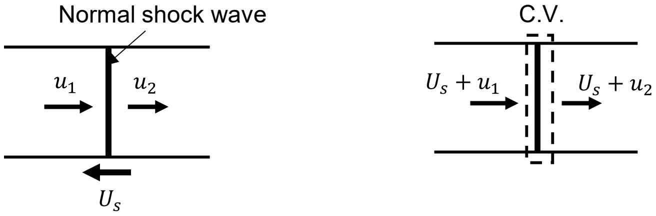

(a) Inertial frame (b) Frame moving with the shock wave

Figure 14: Frame for the moving shock wave

The positions of the terminal shock wave at each time are obtained by calculating U_s using Eq. (10) and Eq. (11). In this calculation, $u_1$and T_1 (for calculation of a_1) at each shock position are obtained by CFD. Here, the distributions of the physical properties upstream of the terminal shock wave is assumed to be unaffected by the time and the surface averaged values at the beginning of I2 obtained by CFD are substituted. Also, the average value of u_{back} during I2 obtained by CFD is substituted in u_2.

During I2, the terminal shock wave changes from the normal shock wave into the shock train. While the terminal shock wave is the normal shock wave, p_{back} at each time is calculated by Eq. (12) hypothesizing the equality between p_2 and p_{back}. In this calculation, p_1 is obtained in a similar manner to $u_1$and T_1. The terminal shock wave changes into the shock train at 1.4 ms according to the result of CFD. After that, p_{back} is fixed at the value calculated just before the terminal shock wave changes into the shock train.

When the calculated shock position reaches the root of the 3rd ramp, the buzz phase is judged to be the start of I3 based on the buzz characteristics indicated in Sec. 3.2. During I3, p_{back} increases at almost the same speed with that of p_{ave} as shown in Fig. 7. In this model, p_{ave} is calculated by the method explained in Sec. 4.1, so the increasing speed of p_{ave} is already known. Therefore, p_{back} during I3 is calculated by setting the increasing speed of p_{back} to be the same with that of p_{ave}.

4.3 Outputs of the model and the discussion

ρ_{ave} and p_{ave} calculated by the methods explained in Sec. 4.1 are shown in Fig. 15 and Fig. 16. Both ρ_{ave} and p_{ave} calculated by the newly constructed model agreed well with the results of CFD. Therefore, these average values inside the intake are shown to be estimated by the mass conservation law. The result of calculating p_{back}, $\dot{m}_{out}$, and the terminal shock wave position using the method explained in Sec. 4.2 are shown in Fig. 16 to Fig. 18. As shown in these graphs, the value of p_{back} and the position of the terminal shock wave during I2 agreed well with those obtained by CFD. Therefore, p_{back} and the position of the head of the terminal shock wave are shown to be governed by the governing equations of the moving normal shock wave while the terminal shock wave is the normal shock wave and the buzz phase is I2, respectively. In addition, the model succeeds in estimating the transition timing to I3 by estimating the timing that the terminal shock wave reaches the root of the 3rd ramp. In regard to I3, p_{back} is shown to be dominated by the mass conservation law from the correspondence of the model output and the result of CFD. With respect to the movement of the terminal shock wave, the previous research [14] showed that the movement becomes faster with the smaller outflow rate (smaller *NOR*) during I3. The cause of this phenomenon seems to be that the pressure inside the intake should increase rapidly with the smaller outflow rate considering the mass conservation law. Therefore, the movement of the terminal shock wave during I3 is also suggested to be governed by the mass conservation law. In conclusion, the newly constructed model is demonstrated to be able to reproduce the shock wave movement and the pressure waveform of the pressure increasing period.

However, one of the problems of this model is related to the accuracy because the error can occur in p_{back} during I2. The reason of this error seems to be that the distribution of the quantities upstream of the terminal shock wave varies with time in reality although this dependence is ignored in the new model. This discrepancy can result in the errors in u_1, T_1, and p_1 and can cause the estimation error in p_{back}. Therefore, other methods that estimate the value of p_{back} during I2, especially while p_{back} is kept almost constant (from 1.2 ms to 2.7 ms), is required to construct the more accurate model.

DOI: 10.13009/EUCASS2023-321

The second problem is the criteria for determining the transition to the pressure decreasing period. As shown in Fig. 15, a little discrepancy exists between the model output and the result of CFD in terms of ρ_{ave}. This discrepancy is caused by the ignorance of the plenum chamber volume. The plenum chamber is the area over the 2nd ramp and the 3rd ramp, and the volume is 3.0×10^{-5} m^3, while the intake flow path volume is 3.0×10^{-4} m^3. The outputs of the modified model considering the plenum chamber volume when calculating the Eq. (4) are also shown in Fig. 15 and Fig. 16. As shown in these graphs the ignorance of the plenum chamber volume does not give a great influence on the waveforms of the pressure and the density. However, the estimated length of the pressure increasing period is changed by 13.5 pt. This change indicates that determining the end of the pressure increasing period based on the maximum p_{ave} is susceptible to the errors. Therefore, other methods to determine the end of the pressure increasing period must be applied to enhance the estimation of the length of the pressure increasing period.

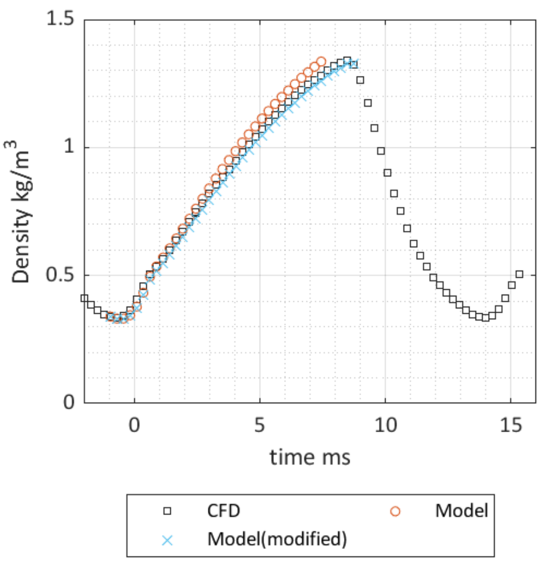

Figure 15: Output of the model (Average density inside the intake)

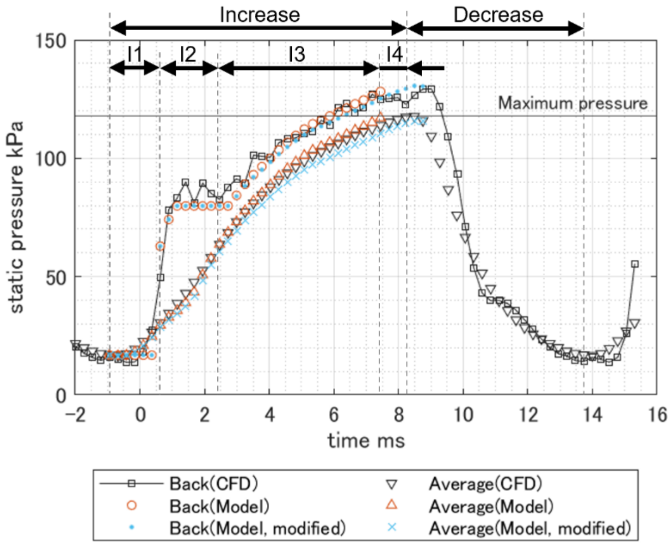

Figure 16: Output of the model (Average static pressure inside the intake and the intake back pressure)

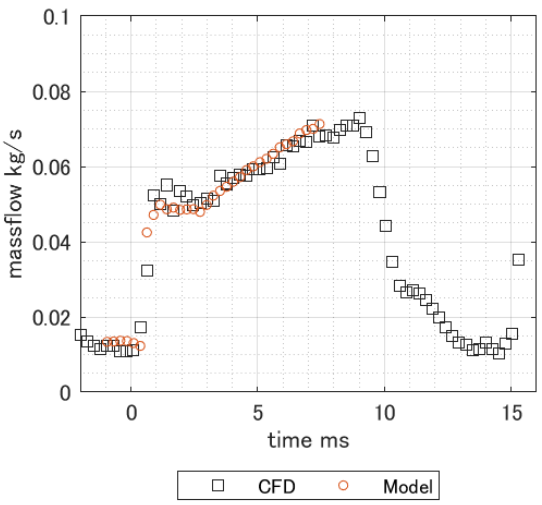

Figure 17: Output of the model (Outflow rate)

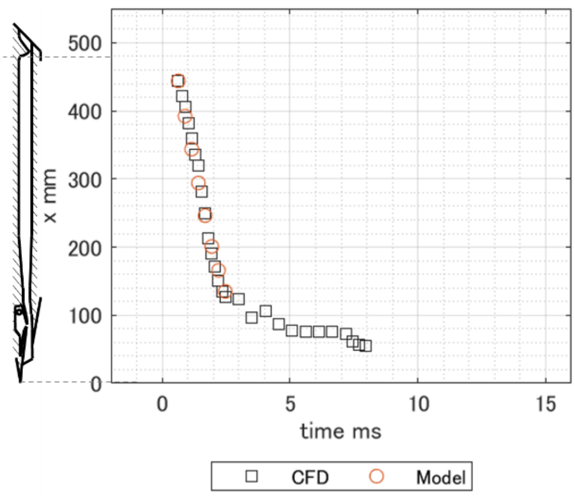

Figure 18: Output of the model (Position of the terminal shock wave)

DOI: 10.13009/EUCASS2023-321

5. Conclusion

In this paper, we have constructed the new buzz model which can reproduce the shock wave movement and the pressure waveform during the pressure increasing period of the buzz occurring in the ramjet intake for HIMICO. In the process, we showed the following things.
a) The high-pressure region expands from the rear part of the intake during the pressure increasing period of the buzz because the inflow rate exceeds the outflow rate. In this period, the terminal shock wave moves upstream inside the intake accompanied with the expansion of the high-pressure region.
b) During the former part of the pressure increasing period (I2), the high-pressure region expands and the terminal shock wave moves upstream from the rear part of the intake to the root of the third ramp. In this period, the pressure of the high-pressure region does not increase very much. In the latter part of the pressure increasing period (I3), the pressure of the high-pressure region increases and the terminal shock wave moves from the root of the 3rd ramp to the intake throat.
c) The newly constructed model which is composed of the governing equations of the moving normal shock wave and the mass conservation law was demonstrated to reproduce the pressure waveform and the movement of the terminal shock wave during the pressure increasing period.
d) During I2, the dominant mechanism of the movement of the terminal shock wave was shown to be the governing equations of the moving normal shock wave. Also, the time change of the intake back pressure was indicated to be also dominated by the governing equations of the moving normal shock wave until the terminal shock wave changes into the shock train.
e) The transition timing from I2 to I3 was successfully estimated by the newly constructed model by estimating the time that the terminal shock wave reaches the root of the 3rd ramp.
f) The dominant mechanism of the intake back pressure during I3 was shown to be the mass conservation law. Also, the movement of the terminal shock wave becomes faster with smaller outflow rate during I3, so the movement of the terminal shock wave is also seemed to be governed by the mass conservation law.

Acknowledgements

This work was supported by JSPS KAKENHI Grant Number JP20H05654 and JP22J21564. We used JAXA Supercomputer System generation 3 (JSS3). Wind tunnel experiments were conducted at the 0.6m x 0.6m transonic/supersonic wind tunnel facility provided by Institute of Space and Astronautical Science, Japan Aerospace Exploration Agency as an inter-university research institute facility (Project ID: W17-013).

References

[1] Early Look: This aircraft concept shows a hypersonic vehicle for passengers, https://www.boeing.com/features/2018/06/hypersonic-concept-vehicle.page
[2] SABRE. The engine that changes everything. https://reactionengines.co.uk/advanced-propulsion/sabre/
[3] Taguchi, H., Kobayashi, H., Kojima, T., Ueno, A., Imamura, S., Hongoh, M., and Harada, K. 2012. Research on hypersonic aircraft using pre-cooled turbojet engines. Acta Astronautica. Vol. 73, pp. 164-172. 10.1016/j.actaastro.2011.10.006
[4] Newsome, R. W. 1984. Numerical Simulation of Near-Critical and Unsteady, Subcritical Inlet Flow. AIAA Journal. Vol. 22, No. 10, pp. 1375-1379. 10.2514/3.48577
[5] Soltani, M. R. and Younsi, J. S. 2016. Buzz Cycle Description in an Axisymmetric Mixed-Compression Air Intake. AIAA Journal. Vol. 54, No. 3, pp. 1036-1049. 10.2514/1.J054215
[6] Berto, F., Benini, E. Wyatt, C., and Quinn, M. K. 2020. Time-Accurate Experimental Investigation of Hypersonic Inlet Buzz at Mach 5. AIAA Journal. Vol. 58, No. 5, pp. 2197-2205. 10.2514/1.J058764
[7] Chen, H., Tan, H., Zhang, Q., and Zhang, Y. 2018. Throttling Process and Buzz Mechanism of a Supersonic Inlet at Overspeed Mode. AIAA Journal. Vol. 56, No. 5, pp. 1953-1964. 10.2514/1.J056674
[8] Myokan, M., Kubota, A., Iwakawa, A., and Sasoh, A. 2020. Repetitive Energy Deposition at a Supersonic Intake in Subcritical and Buzz Modes. AIAA Journal. Vol. 58, No. 1, pp. 107-117. 10.2514/1.J058519
[9] Trapier, S., Duveau, P., and Deck, S. 2006. Experimental Study of Supersonic Inlet Buzz. AIAA Journal. Vol. 44, No. 10, pp. 2354-2365. 10.2514/1.20451

DOI: 10.13009/EUCASS2023-321

[10] Tan, H. J., Sun, S., and Yin, Z. L. 2009. Oscillatory Flows of Rectangular Hypersonic Inlet Unstart Caused by Downstream Mass-Flow Choking. Journal of Propulsion and Power, Vol. 25, No. 1, pp. 138-147. 10.2514/1.37914

[11] Zhang, Q. F., Tan, H. J., Sun, S., Bu, H. X., and Rao, C. Y. 2016. Unstart of a Hypersonic Inlet with Side Compression Caused by Downstream Choking. AIAA Journal. Vol. 54, No. 1, pp. 28-38. 10.2514/1.J054095

[12] Devaraj, M. K. K., Jutur, P., Rao, S. M. V., Jagadeesh, G., and Anavardham, G. T. K. 2021. Length scale for the estimation of buzz frequency in the limit of high mechanical blockage in mixed-compression intakes. Journal of Fluid Mechanics. Vol. 916, No. R3. 10.1017/jfm.2021.230

[13] Sekar, K. R., Karthick, S. K., Jegadheeswaran, S., and Kannan, R. 2020. On the unsteady throttling dynamics and scaling analysis in a typical hypersonic inlet–isolator flow. Physics of Fluids. Vol. 32, No. 126104. 10.1063/5.0032740

[14] Fujii, M., Hoshiya, Y., Fujimori, Y., Kuwabara, Y., Tanaka, R., Ariyoshi, S., Suzuki, A., Sato, T., Taguchi, H., and Hashimoto, A. 2023. Numerical Investigation on the Effects of the Exit Nozzle Throat Height on the Buzz Characteristics Occurring in the Hypersonic Intake for High Mach Integrated Control Experiment (HIMICO). In: Asian Joint Conference on Propulsion and Power 2023. AJCPP2023-105.

[15] Hashimoto, A., Murakami, K., Aoyama, T., Ishiko, K., Hishida, M, Sakashita, M., and Lahur, P. R. 2012. Toward the Fastest Unstructured CFD Code "FaSTAR." In: AIAA Aerospace Sciences Meeting including the New Horizons Forum and Aerospace Exposition. AIAA 2012-1075. 10.2514/6.2012-1075

[16] Spalart, P. R. and Rumsey, C. L. 2007. Effective Inflow Conditions for Turbulence Models in Aerodynamic Calculations. AIAA Journal. Vol. 45, No. 10, pp. 2544-2553. 10.2514/1.29373.

[17] Shima, E., and Kitamura, K. 2011. Parameter-Free Simple Low-Dissipation AUSM-Family Scheme for All Speeds. AIAA Journal. Vol.49, No.8, pp. 1693-1709. 10.2514/1.J050905.

[18] Hishida, M., Hashimoto, A., Murakami, K., and Aoyama, T. 2010. A new slope limiter for fast unstructured CFD solver FaSTAR. In: The 42nd Fluid Dynamics Conference/ Aerospace Numerical Simulation Symposium 2010. JAXA-SP-10-012.